

Accelerating Volumetric Medical Image Annotation via Short-Long Memory SAM 2

Yuwen Chen, Zafer Yildiz, Qihang Li, Yaqian Chen, Haoyu Dong, Hanxue Gu, Nicholas Konz, Maciej A. Mazurowski

Abstract—Manual annotation of volumetric medical images, such as magnetic resonance imaging (MRI) and computed tomography (CT), is a labor-intensive and time-consuming process. Recent advancements in foundation models for video object segmentation, such as Segment Anything Model 2 (SAM 2), offer a potential opportunity to significantly speed up the annotation process by manually annotating one or a few slices and then propagating target masks across the entire volume. However, the performance of SAM 2 in this context varies. Our experiments show that relying on a single memory bank and attention module is prone to error propagation, particularly at boundary regions where the target is present in the previous slice but absent in the current one. To address this problem, we propose Short-Long Memory SAM 2 (SLM-SAM 2), a novel architecture that integrates distinct short-term and long-term memory banks with separate attention modules to improve segmentation accuracy. We evaluate SLM-SAM 2 on three public datasets covering organs, bones, and muscles across MRI and CT modalities. We show that the proposed method markedly outperforms the default SAM 2, achieving average Dice Similarity Coefficient improvement of 0.14 and 0.11 in the scenarios when 5 volumes and 1 volume are available for the initial adaptation, respectively. SLM-SAM 2 also exhibits stronger resistance to over-propagation, making a notable step toward more accurate automated annotation of medical images for segmentation model development.

Index Terms—Medical Image Annotation, SAM 2, Deep Learning, Segmentation

I. INTRODUCTION

SEMANtic segmentation plays a crucial role in medical image analysis, serving as a foundational step in numerous clinical and research applications, including tumor identification and measurement, treatment planning, and body composition analysis [1]–[3]. With advances in computer vision, deep

learning-based methods (e.g., UNet [4]) have increasingly become the dominant approach for medical image segmentation due to their superior robustness and efficiency. However, developing reliable deep learning models often demands high-quality manual annotations, which are time-consuming and expensive to acquire [5], particularly for 3-dimensional (3D) volumetric medical data (e.g., MRI and CT) that consist of numerous 2D slices, requiring detailed labeling.

3D medical imaging data typically consists of a stack of 2D slices acquired along an additional spatial axis. These 2D consecutive slices are often highly correlated, capturing gradual anatomical changes across the axis. Consequently, the 3D volume data can be interpreted as a temporal progression, analogous to frames in a video [6], [7]. Leveraging such similarity between adjacent slices offers an effective method to accelerate annotation process by propagating annotations from a single slice to the rest of the volume [6]–[11].

Several approaches have employed self-supervised learning (e.g., training registration networks) to learn semantic correspondences between adjacent slices. These correspondences are subsequently utilized to propagate annotations from a labeled slice to neighboring slices for segmentation [8]–[11]. However, these methods are prone to *error drift*, where errors accumulate during propagation. Furthermore, they exhibit limitations in handling discontinuities within 3D volumes, such as the emergence of previously unseen anatomical structures or the disappearance of existing ones [11].

The recently developed video object segmentation (VOS) foundation model, Segment Anything Model 2 (SAM 2) [12], has been applied to medical imaging segmentation [6], offering an alternative. Vision foundation models have demonstrated exceptional generalization capabilities without requiring access to large-scale labeled datasets [2], [13], [14]. Through extensive pretraining, these models acquire robust and adaptable feature representations, which facilitate their applications to downstream tasks with limited annotated data [2]. In VOS tasks, the objective is to track objects throughout a video sequence by propagating an initial object mask provided in the first frame [12], [15]. By interpreting the depth dimension as the temporal axis, SAM 2 offers a supervised method (i.e., training with images and corresponding masks) to propagate annotation masks across slices. For instance, SAM 2 has been utilized to build a 3D interaction framework [7], and an extension based on SAM 2 has been developed and integrated into 3D Slicer to facilitate the annotation of 3D volumes [16].

Manuscript submitted on May 3. This work was supported by the National Institute Of Biomedical Imaging And Bioengineering of the National Institutes of Health under Award Number R01EB031575.

Yuwen Chen, Yaqian Chen, Haoyu Dong, Hanxue Gu, Nicholas Konz are with the Department of Electrical and Computer Engineering, Duke University, Durham, NC 27708 USA (e-mail: yuwen.chen@duke.edu; yaqian.chen@duke.edu; haoyu.dong151@duke.edu; hanxue.gu@duke.edu; nicholas.konz@duke.edu)

Zafer Yildiz and Qihang Li are with the Department of Biostatistics and Bioinformatics, Duke University, Durham, NC 27708 USA (e-mail: zafer.yildiz@duke.edu; qihang.li@duke.edu)

Maciej A. Mazurowski is with Department of Biostatistics and Bioinformatics, Radiology, Electrical and Computer Engineering, and Computer Science, Duke University, Durham, NC 27708 USA (e-mail: maciej.mazurowski@duke.edu)

Based on SAM [13], SAM 2 enables video object segmentation by introducing a memory encoder, memory bank, and memory attention [12]. The memory encoder constructs memory representation through element-wise summation of encoded images and their corresponding output masks. The memory bank serves as a repository that retains information and past predictions from N recent slices and M prompted slices. Additionally, the memory attention module enhances the feature representation of the current slice by conditioning it on the features and predictions of past slices from the memory bank. The output features from the memory attention are then input to the mask decoder to generate mask prediction.

Nevertheless, our experiments (Sec. IV-E) reveal that SAM 2, under its default settings ($N + M = 7$), exhibits suboptimal performance at discontinuous slice boundaries, particularly during object disappearance or emergence. The limitations can be attributed to two primary factors: (1) persistent retention of prompted slices in the memory bank throughout the entire propagation, which can introduce outdated or irrelevant context, and (2) reliance on multiple recent slices ($N \geq 5$), which may result in over-segmentation due to the accumulation of momentum from prior frames. These issues highlight the need for a more adaptive memory mechanism that can effectively keep temporal consistency while maintaining sufficient flexibility to address abrupt changes and discontinuities.

Intuitively, a longer memory (i.e., larger N) allows the model to track gradual changes in the object, thereby enhancing the stability and continuity of predictions over slices. In contrast, a shorter memory (i.e., smaller N) emphasizes the most recent slices, improving the model's adaptability to discontinuous changes in object appearance. To leverage the complementary advantages of both long-term and short-term memory, we propose **Short-Long Memory SAM 2 (SLM-SAM 2)**¹, a novel framework that incorporates two memory banks, one long-term and one short-term, to achieve more robust and accurate segmentation. We validate the effectiveness of SLM-SAM 2 through experiments on three public datasets spanning both MRI and CT modalities. The results demonstrate that SLM-SAM 2 significantly outperforms existing 2D and 3D segmentation methods. Our contributions are summarized below:

- We propose a novel architecture, SLM-SAM 2, which leverages the complementary strengths of long-term and short-term memory to facilitate and enhance 3D medical image annotations.
- Our method significantly outperforms existing approaches in segmenting organs, bones, and muscles across both MRI and CT modalities, achieving an average dice score improvement of at least 7% across different datasets.
- We demonstrate both qualitatively and quantitatively that SLM-SAM 2 can effectively alleviate the over-propagation issue.
- We integrate SLM-SAM 2 into 3D Slicer and release the extension to facilitate 3D medical data annotation.

II. RELATED WORK

A. Semantic Segmentation in Medical Imaging

Semantic segmentation aims to classify each pixel in an image, making it an essential task in both natural and medical imaging [17], [18]. Convolutional Neural Networks (CNNs) have been a dominant approach for vision tasks, with UNet [4] emerging as a widely adopted model in medical image segmentation. The skip connections between encoder and decoder allows UNet to effectively capture both global and local context. Building on UNet, nnUNet [19] introduces a fully automated training pipeline configuration, which can be efficiently adapted to any new medical segmentation tasks. Nevertheless, one of the key limitations of CNNs is that they often struggle to capture long-range dependencies [20].

To overcome this issue, Vision Transformers (ViTs) employ a transformer architecture that divides images into sequence of patches [21]. The self-attention mechanism in ViTs allows them to capture global context, enhancing segmentation accuracy for anatomies with large receptive fields (e.g., the liver). Recently, vision foundation models, such as SAM [16], have further advanced the medical image segmentation. SAM leverages a transformer-based encoder and extensive pretraining on large-scale datasets, enabling exceptional generalization capabilities across multiple downstream tasks with minimal labeled data [22], [23].

B. Video Object Segmentation (VOS)

Video object segmentation focuses on segmenting particular object instance given an entire video sequence and an object mask on the first frame, either manual annotated or automatically generated [15]. VOS has numerous applications in various domains, including autonomous vehicles [24], [25], robotics [26], [27] and medical imaging analysis [6], [28]. VOS methods can be broadly categorized into unsupervised VOS and semi-supervised VOS [29]. Unsupervised VOS aims to identify and segment the most salient objects in a video without any given annotations. In contrast, semi-supervised VOS requires initial annotations, which are typically provided in the first frame [30].

Recently, several novel approaches, such as Cutie [31] and SAM 2 [12], have been introduced for semi-supervised VOS tasks. Cutie employs an iterative interaction between top-down object-level memory reading and bottom-up pixel-level features to effectively capture the semantic structure of foreground objects [31]. SAM 2 incorporates a pretrained ViT backbone along with a memory mechanism that includes a memory bank, memory encoder, and memory attention module [12]. The enriched feature representations from the pretrained ViT encoder allow SAM 2 to achieve robust generalization performance across different tasks.

C. Medical Image Annotation for Segmentation

Medical image annotation for segmentation tasks involves pixel-level labeling of images across various modalities to train deep learning-based segmentation models [32]. The manual annotation process is both expensive and time-consuming due to the complexity of different modalities and anatomical

¹GitHub at: <https://github.com/mazurowski-lab/SLM-SAM2>

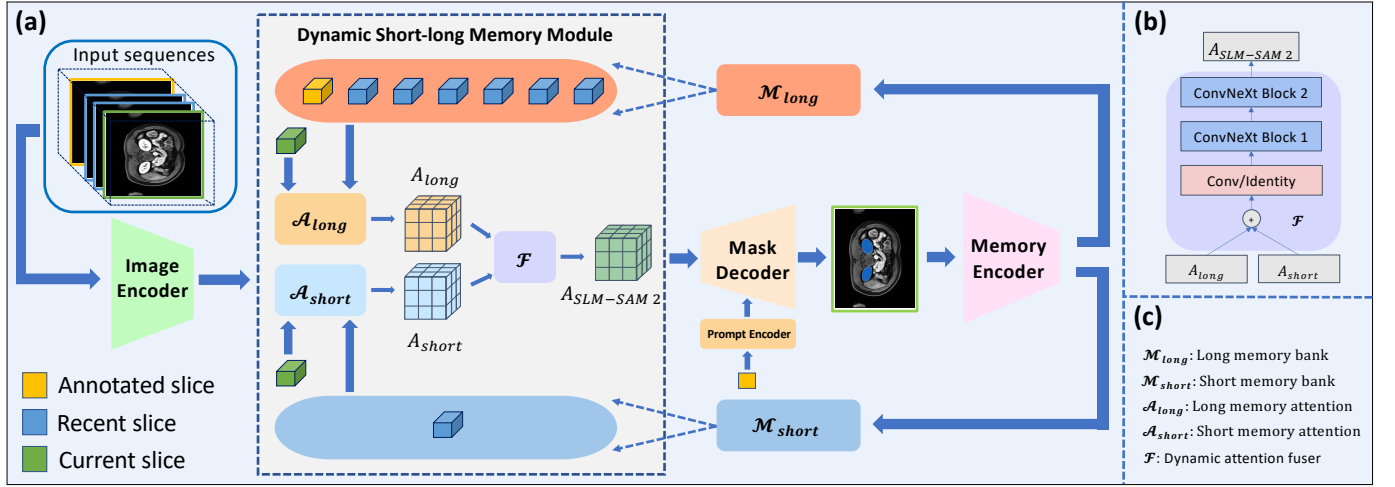


Fig. 1. Overview of SLM-SAM 2. (a) is the general pipeline of SLM-SAM 2. The dynamic short-long memory module consists of short-term and long-term memory banks (\mathcal{M}_{short} and \mathcal{M}_{long}), two distinct attention modules for each of them (\mathcal{A}_{short} and \mathcal{A}_{long}), and the dynamic attention fuser (\mathcal{F}). Specifically, \mathcal{M}_{long} includes one annotated slice and up to six additional slices, while \mathcal{M}_{short} contains only the most recent slice. (b) illustrates the architecture of the dynamic attention fuser \mathcal{F} . (c) provides an explanation of the key notations used in SLM-SAM 2.

structures [33], [34]. Moreover, a significant portion of medical images is acquired in three-dimensional formats, including MRI, CT, and video-based imaging (e.g., colonoscopy and ultrasound), further increasing the annotation workload.

To address these challenges, various approaches have been developed, which can be broadly categorized into unsupervised, supervised and interactive methods. Unsupervised methods focus on learning spatial relationship between adjacent slices in 3D data, enabling label propagation from a single annotated slice to entire volume during inference [8], [11]. However, these methods are prone to error drift [11]. Supervised methods often utilize few-shot learning [35], [36], where a model is trained on a small, fully annotated subset data before being applied to the remaining data. This category involves 2D [37], [38], 3D [39], [40], and VOS models [12], [31], with VOS technique sometimes requiring minimal annotations during the inference stage. Interactive annotation methods integrate automated predictions with real-time human corrections, enabling quick refinement of initial annotations, and thus improving annotation efficiency [35], [41].

III. METHODS

This work aims to develop robust and reliable slice propagation models that can accelerate annotation of volumetric medical image data. In this section, we define the problem and introduce the proposed SLM-SAM 2 in detail.

A. Problem Definition

Given a fully annotated volume set $\{X_i | i = 0, \dots, n\}$ for training, the objective is to segment any incoming volumes from $\{Y_i | i = 0, \dots, m\}$ by annotating a single slice from each volume. In this study we chose $n = 5$, reflecting a practical setting in which users initially provide full annotations for a limited number of volumes and subsequently annotate only one slice for each newly acquired volume.

B. Model Architecture of SLM-SAM 2

Fig. 1 (a) depicts the overall SLM-SAM 2 pipeline. SLM-SAM 2 retains the foundational architecture of SAM 2, including the image encoder E_I , prompt encoder E_P , and mask decoder D . In SAM 2, at slice s_i , the memory attention A_{SAM2} can be simply expressed as:

$$A_{SAM2} = \mathcal{A}(E_I(s_i), [E_M(s_j) | s_j \in \mathcal{M}]) \quad (1)$$

where E_M is the memory encoder and \mathcal{M} is the memory bank. We use the SAM 2 “tiny” model architecture in this work.

The key dynamic short-long memory module consists of a short-long memory bank mechanism and a dynamic attention fuser, as described below.

1) Short-long Memory Bank: Similar to SAM 2, SLM-SAM 2 inputs the new incoming slices to the image encoder to generate the corresponding feature representations. To enable both short-term and long-term memory storage, SLM-SAM 2 introduces an additional memory bank and memory attention. The long-term memory bank \mathcal{M}_{long} follows the original SAM 2 design by storing N_{long} recent and M_{long} prompted slices, ensuring continuity in segmentation. The short-term memory bank \mathcal{M}_{short} solely retains the most recent N_{short} slice, where N_{short} is a typically small positive integer, allowing model predictions to quickly adapt to abrupt object changes. During propagation, the conditions of the current slices on both short-term and long-term memory, \mathcal{A}_{short} and \mathcal{A}_{long} , are computed independently through two memory attention modules, \mathcal{A}_{short} and \mathcal{A}_{long} , respectively.

$$A_{short} = \mathcal{A}_{short}(E_I(s_i), [E_M(s_j) | s_j \in \mathcal{M}_{short}]) \quad (2)$$

$$A_{long} = \mathcal{A}_{long}(E_I(s_i), [E_M(s_j) | s_j \in \mathcal{M}_{long}]) \quad (3)$$

The two memory modules are of the same architecture, resulting in output attentions of the same size. Specifically, SLM-SAM 2 uses $N_{long} = 6$, $M_{long} = 1$ and $N_{short} = 1$.

Algorithm 1: SLM-SAM 2 Training Pseudo-Code**Input:** $D = \{(I_{\text{seq}}, M_p, S_{\text{seq}}^{\text{gt}})\}$: Training data sequences $I_{\text{seq}} = \{I_1, I_2, \dots, I_T\}$: Sequence of T frames P : Mask prompt $S_{\text{seq}}^{\text{gt}} = \{S_1^{\text{gt}}, S_2^{\text{gt}}, \dots, S_T^{\text{gt}}\}$: Ground-truth masks N : Number of training epochs.**Output:** Trained model parameters.

```

1 for epoch  $\leftarrow 1$  to  $N$  do
2   for each  $(I_{\text{seq}}, P, S_{\text{seq}}^{\text{gt}})$  in  $D$  do
3      $\mathcal{M}_{\text{long}} \leftarrow \emptyset$ ; // long-term memory
4      $\mathcal{M}_{\text{short}} \leftarrow \emptyset$ ; // short-term memory
5      $F_P \leftarrow E_P(P)$ ;
6      $L_{\text{total}} \leftarrow 0$ ;
7     for  $t \leftarrow 1$  to  $T$  do
8       // Forward pass
9        $F_I \leftarrow E_I(I_t)$ ;
10       $A_{\text{long}} \leftarrow \mathcal{A}_{\text{long}}(E_I, \mathcal{M}_{\text{long}})$ ;
11       $A_{\text{short}} \leftarrow \mathcal{A}_{\text{short}}(E_I, \mathcal{M}_{\text{short}})$ ;
12       $A_{\text{SLM-SAM2}} \leftarrow \mathcal{F}(A_{\text{long}}, A_{\text{short}})$ ;
13       $(S_t^{\text{pred}}, Q_t^{\text{pred}}) \leftarrow D(A_{\text{SLM-SAM2}}, F_P)$ ;
14      // Compute loss
15      Compute  $L_{\text{step}}$ ;
16       $L_{\text{total}} \leftarrow L_{\text{total}} + L_{\text{step}}$ ;
17      // Update memory
18       $F_M \leftarrow E_M(I_t, S_t^{\text{pred}})$ ;
19       $\mathcal{M}_{\text{long}} \leftarrow \text{UPDATE}(\mathcal{M}_{\text{long}}, F_M)$ ;
20       $\mathcal{M}_{\text{short}} \leftarrow \text{UPDATE}(\mathcal{M}_{\text{short}}, F_M)$ ;
21 RESET_GRADIENTS();
22 BACKPROPAGATE( $L_{\text{total}}$ );
23 OPTIMIZER_STEP();
24 return Trained model parameters.

```

2) Dynamic Attention Fuser: The two output attentions are subsequently fused using a lightweight, learnable fusion module \mathcal{F} . It contains an optional projection layer followed by two ConvNeXt blocks [42], as shown in Fig. 1 (b).

$$A_{\text{SLM-SAM2}} = \mathcal{F}(A_{\text{short}}, A_{\text{long}}) \quad (4)$$

The fused attention $A_{\text{SLM-SAM2}}$ is of the same shape as A_{SAM2} , allowing it to be directly fed into the mask decoder to generate output predictions. All newly introduced modules adopt the same architecture as the original SAM 2 components to leverage the pretrained weights.

C. Annotation Propagation via SLM-SAM 2

The finetuning process of SLM-SAM 2 is described in Algorithm 1. The loss function incorporates focal loss, Dice loss, MAE loss for IoU prediction, and cross-entropy loss, with weights the same as those used in SAM 2 [12]. At inference, the central slice of the object of interest is selected as the initial annotation point, and the mask is propagated in a bi-directional manner, first toward one direction and subsequently

in the opposite direction. To enhance the model's ability to track the object in both directions, we randomly flip half of the sequence order during training.

IV. EXPERIMENTS

We have performed a thorough evaluation of the proposed SLM-SAM 2. In this section, we describe datasets, implementation details, and baselines, followed by results including ablation studies to verify the key designs of SLM-SAM 2.

A. Datasets

We evaluated SLM-SAM 2 on three publicly available datasets spanning different imaging modalities, covering anatomical structures including organs, bones, and muscles.

1) Organ Segmentation: We used AMOS dataset [43] to segment the kidneys and pancreas in MRI scans (MRI-Kidney and MRI-Pancreas) and the pancreas and spleen in CT scans (CT-Pancreas and CT-Spleen), with 25 volumes randomly selected for each modality. Heart segmentation was performed on the CT dataset from the TotalSegmentator project [41] (CT-Heart), using 35 randomly selected volumes for each task.

2) Bone Segmentation: We assessed CT femur segmentation task on randomly selected 35 volumes from the TotalSegmentator project [41] (CT-Femur).

3) Muscle Segmentation: The HuashanMyo MRI dataset [44] was used to evaluate muscle segmentation on the gracilis and sartorius muscles (MRI-Gracilis and MRI-Sartorius), with 25 randomly selected volumes.

In all experiments, 5 volumes from each dataset were randomly chosen for training, and the remaining volumes were used for testing. All 2D slices were extracted from axial view.

B. Implementation Details

We followed the default settings of SAM 2 for end-to-end finetuning SLM-SAM 2, with the exception that only mask prompts were utilized, given that our study focuses on VOS tasks. The batch size was set to 1, and each input sequence was composed of 8 randomly selected consecutive 2D slices. For each segmentation task, the model was finetuned using the AdamW optimizer for 100 epochs. All models were trained on a single NVIDIA GeForce RTX A6000. The initial learning rates for the image encoder and the remaining model components were set to 3×10^{-6} and 5×10^{-6} , respectively, and were updated using a cosine annealing scheduler. All 2D images were resized to a resolution of 1024 and normalized to a range of 0 to 255 at the volume level². The training data augmentation pipeline followed the SAM 2 implementation.

C. Baseline Methods

To evaluate the effectiveness of SLM-SAM 2, we compared its segmentation performance against state-of-the-art VOS models, including SAM 2 [12] and Cutie [31]. Additionally, we assessed its performance relative to leading 2D and 3D

²For CT scans, intensities were clipped to the range [-1024, 2000] in Hounsfield Units (HU)

fully automated segmentation models, such as nnUNet [19], UNETR [39] and Swin UNETR [40]. We also compared our performance against unsupervised VOS methods, including VoxelMorph [45] and Sli2Vol [8]. Cutie leverages a query-based object transformer to integrate top-down object-level memory with bottom-up pixel-level features, segmenting foreground targets through the foreground-background masked attention. Cutie+, a variant of Cutie with larger memory bank that offers improved performance but with slower inference speed, is also included. We chose base model for Cutie and Cutie+, initialized with pretrained weights, and followed the default training settings from official GitHub. nnUNet is a robust, self-adapting framework based on the UNet architecture [4]. We evaluated the 2D nnUNet in two settings: the basic (B) and the exhaustive (E) setting. In the basic setting, the model was trained on n fully annotated volumes and evaluated directly on the test set. In the exhaustive setting, we retrained a model individually for each test volume, using n fully annotated volumes along with one annotated slice from that test volume. UNETR and SwinUNETR are state-of-the-art 3D transformer-based medical image segmentation models. UNETR employs a pure transformer encoder for volumetric representation learning, while Swin UNETR utilizes swin transformer-based blocks for enhanced feature extraction. All 3D models were trained on n fully annotated volumes using the AdamW optimizer with an initial learning rate of 1×10^{-3} .

D. Evaluation Metrics

We quantitatively assessed the performance of SLM-SAM 2 using the Dice Similarity Coefficient (DSC) and Average Symmetric Surface Distance (ASSD), both evaluated on 3D volumetric segmentation. Given the predicted mask A and the ground truth mask B , the two metrics are defined as below:

$$DSC(A, B) = \frac{2|A \cap B|}{|A| + |B|} \quad (5)$$

DSC measures the overlap between A and B , with values ranging from 0 and 1. Higher DSC values indicate better segmentation performance.

$$ASSD(A, B) = \frac{\sum_{p \in S_A} d(p, S_B) + \sum_{q \in S_B} d(q, S_A)}{|S_A| + |S_B|} \quad (6)$$

where S_A and S_B denote the sets of surface points of mask A and B . $d(p, S_B)$ and $d(q, S_A)$ represent the shortest Euclidean distances from a surface point in S_A and S_B to the nearest point in S_B and S_A , respectively. Compared to DSC, ASSD penalizes more on boundary errors. ASSD is non-negative and a lower ASSD indicates better segmentation performance.

For both 5-Volume and 1-Volume setting, we estimated model robustness using bootstrapping with 1,000 resamples. For the 1-Volume setting, we averaged performance from five models per sample. To ensure fair volume-wise evaluation, the predictions on the selected annotated slices are replaced with ground truth for nnUNet (B), UNETR and SwinUNETR.

E. Results

Average performance (DSC & ASSD) across all datasets (5-Volume)

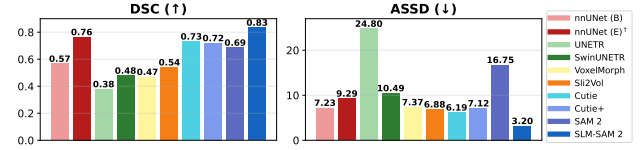


Fig. 2. Average performance comparison across datasets (5-Volume). SLM-SAM 2 demonstrates the best average performance compared among all baselines in both DSC and ASSD.

1) Overall Performance Comparison of SLM-SAM 2: The average performance of SLM-SAM 2 with other baselines is presented in Fig. 2. Overall, we observed that SLM-SAM 2 consistently outperforms the competing methods by a significant margin, achieving improvements of over 0.07 in DSC and 2.99 in ASSD at least. In particular, while SAM 2 achieves a DSC of 0.69, SLM-SAM 2 attains a DSC of 0.83, thereby demonstrating the benefits of incorporating both short-term and long-term memory banks in mask propagation.

VOS methods generally show superior performance in slice propagation tasks while maintaining comparable computational costs. One explanation is both Cutie and SAM 2 are initialized with pretrained weights, leading to outperformance when finetuned on small datasets. Notably, Cutie and Cutie+ slightly outperformed SAM 2, achieving DSC of 0.73 and 0.72, respectively. This is reasonable as Cutie is found to be one of the most competitive methods relative to SAM 2 [12].

The runner-up method, nnUNet (E), requires retraining for each new volume, which leads to a considerable increase in time and computational resources. However, excluding the annotated slice in the training (i.e., nnUNet (B)) results in a significant performance degradation (0.19 reduction in DSC).

The 3D models, UNETR and SwinUNETR, show suboptimal performance with DSC values of 0.38 and 0.48, respectively. One reason could be they do not leverage annotated slice information during either training or inference stages.

Moreover, unsupervised methods, VoxelMorph and Sli2Vol, exhibit lower DSC performance compared to the VOS-based methods. This underperformance can be attributed to the training on unlabeled data, which focuses on learning general information transformation between slices and may not directly learn task-specific features for accurate segmentation.

2) Performance Comparison of Each Dataset/Task: The quantitative results (DSC and ASSD) of SLM-SAM 2 and all competing methods across the datasets/tasks are presented in Table I and Fig. 3. Overall, SLM-SAM 2 outperforms the other baselines in terms of DSC on most datasets. For the CT-Spleen tasks, all VOS methods achieve a DSC of around 0.96, performing comparable to each other. On CT-Heart, SLM-SAM 2 (DSC: 0.7655) underperforms nnUNet (E) (DSC: 0.8013) and slightly underperforms Cutie (DSC: 0.7855). However, nnUNet (E) requires retraining for each new volumes, limiting its scalability. It is notably that SLM-SAM 2 consistently outperforms SAM 2 across organs, bones, and muscles, demonstrating its improved robustness in mask propagation tasks. Moreover, among 2D method, nnUNet (E) consistently outperform nnUNet (B) for all datasets. This is

TABLE I

QUANTITATIVE COMPARISON (DSC AND ASSD) FOR EACH DATASET UNDER THE 5-VOLUME SETTINGS. BEST RESULTS ARE IN BOLD; RUNNER-UP IS UNDERLINED. †: METHOD REQUIRES RETRAINING FOR EACH TEST VOLUME.

	MRI-Kidney		MRI-Pancreas		CT-Pancreas		CT-Spleen		CT-Heart		CT-Femur		MRI-Gracilis		MRI-Sartorius	
Methods	DSC (†)	ASSD (↓)	DSC (†)	ASSD (↓)	DSC (†)	ASSD (↓)	DSC (†)	ASSD (↓)	DSC (†)	ASSD (↓)	DSC (†)	ASSD (↓)	DSC (†)	ASSD (↓)	DSC (†)	ASSD (↓)
I. 2D Models																
nnUNet (B)	0.6497	5.8917	0.3348	8.1976	0.1445	22.6483	0.2731	10.8427	0.6426	<u>7.5425</u>	0.9013	1.8705	0.7083	1.9009	0.6818	1.4850
nnUNet (E)†	<u>0.9073</u>	2.8406	<u>0.6234</u>	8.8195	0.4337	23.2610	0.7548	29.3823	0.8013	9.1686	<u>0.9476</u>	<u>1.5655</u>	0.7843	1.7841	<u>0.7562</u>	<u>1.4003</u>
II. 3D Models																
UNETR	0.4661	22.5008	0.2754	13.3468	0.0320	76.1877	0.1548	51.7418	0.5727	21.5100	0.5524	10.3962	0.4691	3.8774	0.3260	7.7069
SwinUNETR	0.6508	4.6814	0.3778	8.8737	0.1525	13.4887	0.3182	21.0385	0.5937	17.1132	0.5948	8.6549	0.5324	3.9244	0.4981	3.7137
III. Unsupervised VOS Models																
VoxelMorph	0.3854	5.8693	0.2501	13.7858	0.4307	15.6178	0.7806	2.6862	0.5211	6.6286	0.3411	8.3026	0.5707	3.0872	0.5163	2.8654
Sli2Vol	0.8287	<u>1.6272</u>	0.4676	10.9631	0.4636	13.0736	0.7549	5.3969	0.6243	6.3413	0.3042	9.1010	0.5214	3.7066	0.4352	4.0077
IV. Semi-supervised VOS Models																
Cutie	0.8976	1.9001	0.5340	6.6390	0.6806	8.3856	0.9629	0.5550	0.7855	6.2811	0.6303	16.7382	0.7081	2.1894	0.6813	1.5448
Cutie+	0.8997	1.6683	0.5572	6.3690	0.6628	7.7925	0.9574	0.5197	0.7031	12.2835	0.6285	17.0783	0.7209	2.1434	0.6839	1.5357
SAM 2	0.8668	5.9103	0.2341	30.4152	0.6381	9.1385	0.9633	0.4508	0.6925	15.6042	0.6267	52.3565	0.7926	1.4828	0.7045	1.4530
SLM-SAM 2	0.9368	1.3643	0.6294	8.4185	0.7255	4.0753	0.9607	0.4767	0.7655	8.2143	0.9643	0.4298	0.8543	0.7276	0.8118	0.7524

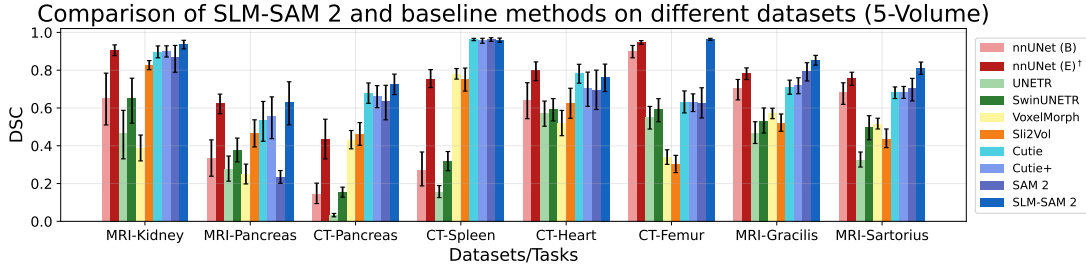


Fig. 3. Performance results (DSC) of each method across datasets (5-Volume). SLM-SAM 2 outperforms all baselines on most datasets by a significant margin. Confidence intervals are estimated using bootstrapping with 1000 resamples.

expected as nnUNet (E) leverages an additional annotated slice from each test volume. For the 3D methods, SwinUNETR demonstrates superior performance compared to UNETR on all datasets. For unsupervised VOS methods, VoxelMorph outperforms Sli2Vol on certain datasets, such as CT-Femur and MRI muscle tasks while Sli2Vol achieves better performance than VoxelMorph on both MRI and CT organ tasks.

Fig. 4 presents the qualitative results of all methods across all datasets. For each dataset, the annotated slices from the selected volume are shown in the leftmost column. The remaining columns display the ground truth and the propagated masks on representative slices. For target-present slices (i.e., slices where target is present), it can be observed that SLM-SAM 2 can achieve a better performance in segmenting small and anatomically challenging structures, such as the MRI-Gracilis and MRI-Sartorius muscles (as shown in Fig. 5 (a)), where accurate delineation is often hindered by low contrast and ambiguous boundaries. For larger and more distinct anatomical structures, including CT-Spleen, CT-Heart and CT-Femur, the segmentation performance of SLM-SAM 2 seems to be comparable to that of some other baselines.

For target-absent slices (i.e., slices where target is absent), SAM 2 and several other VOS methods tends to over-propagate masks of segmentation into regions where the target is no longer present, particularly in adjacent anatomical structures with similar intensity. For instance, in MRI-Kidney, Cutie, Cutie+ and SAM 2 sometimes over-propagate the kidney masks onto the spleen. Similarly, in CT-Femur, other VOS methods may segment the hip bones as the femurs, likely due to their similar appearance and spatial overlap in

axial 2D slices. These challenges are not limited to VOS methods. Competing 2D and 3D segmentation models, such as nnUNet (E), UNETR and SwinUNETR, can also mis-segment adjacent anatomical structures. For example, these models may incorrectly segment the spleen in MRI-Kidney tasks. However, experimental results demonstrate that SLM-SAM 2, which incorporates dynamically learned short-term and long-term memory mechanisms, can effectively alleviate this issue (Fig. 4, Fig. 5 (a) and Fig. 6), leading to more accurate and robust models for slice propagation.

3) *SLM-SAM 2 v.s. SAM 2 on Over-propagation*: We further investigate the benefits of integrating both short-term and long-term memory in SLM-SAM 2, compared to SAM 2. To do this, we compute the 2D slice-wise DSC on target-present slices and target-absent slices, as shown in Fig. 5 (a).

For most datasets except two MRI muscles datasets, SLM-SAM 2 and SAM 2 achieve comparable performance on target-present slices. However, for target-absent slices, SLM-SAM 2 demonstrates significant outperformance compared to SAM 2, with particularly notable improvements observed on MRI-Kidney, MRI-Pancreas, CT-Pancreas and CT-Femur.

Fig. 5 (b)-(e) presents more direct and illustrative results. Specifically, Fig. 5 (b) depicts the 2D DSC over slice index for an example from MRI-Kidney dataset. Figs. 5 (c), (d) and (e) provide qualitative comparison of the segmentation performance between SLM-SAM 2 versus SAM 2 on the selected representative slices in the MRI-Kidney example. Firstly, it can be seen that the 2D DSC on target-present slices is similar between SLM-SAM 2 and SAM 2, as shown in Fig. 5 (c). However, once the kidney is no longer present (i.e.,

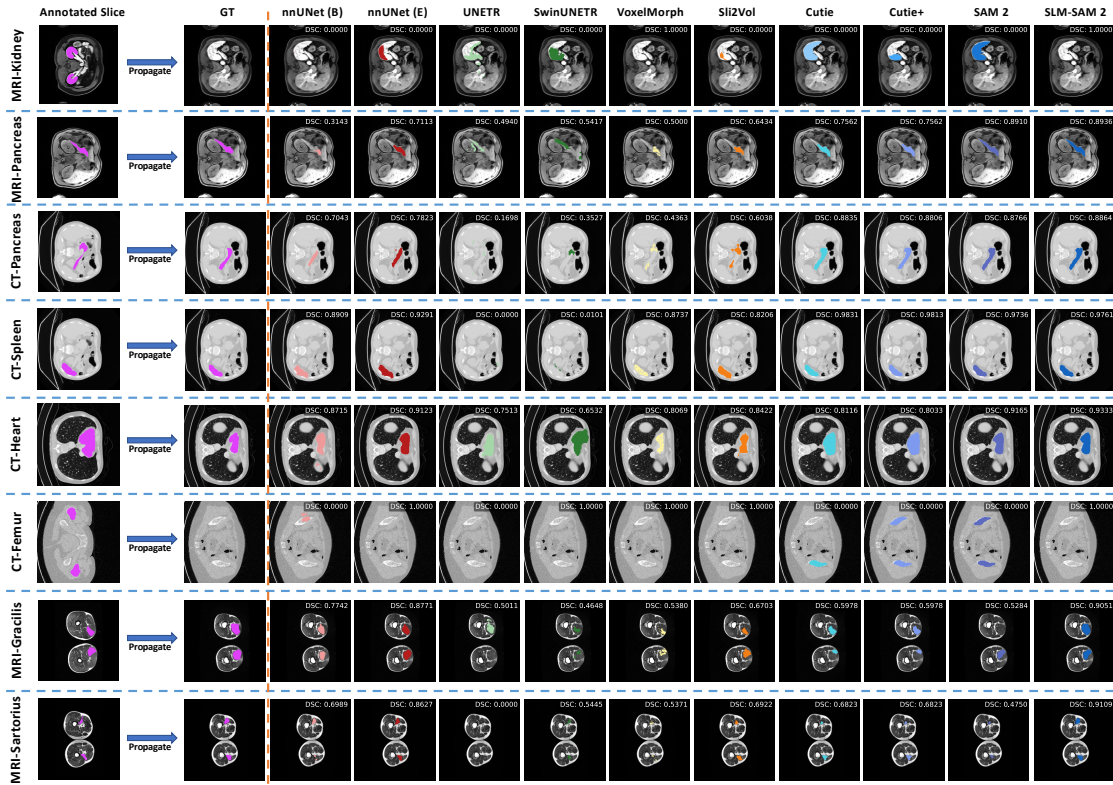


Fig. 4. Qualitative comparison on each dataset (5-Volume). The leftmost column shows the annotated slices, followed by the ground truth (GT) and segmentations from each method. For each dataset, we present results on both target-present and target-absent slices.

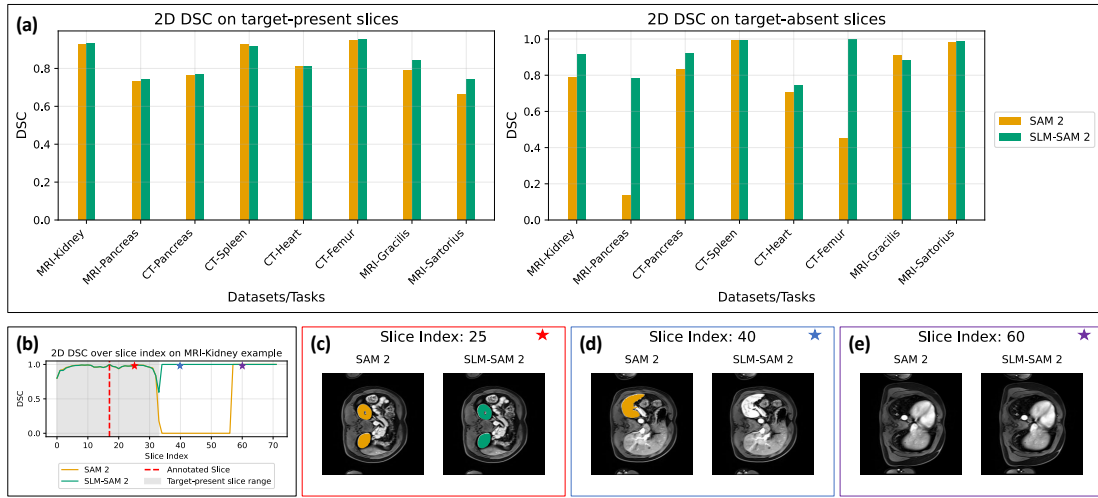


Fig. 5. Performance results on target-present and target-absent slices (5-Volume). (a) presents 2D slice-level DSC for both target-present slices and target-absent slices across datasets. (b) plots 2D slice-level DSC over slice index on an MRI-Kidney example. (c)-(e) provide segmentation comparison between SAM 2 and SLM-SAM 2 on representative slices from the same MRI-Kidney volume.

beyond the gray panel range), the 2D DSC of SAM 2 drops to zero, whereas SLM-SAM 2 maintains a 2D DSC of 1. As illustrated in Fig. 5 (d), this is because SAM 2 over-propagates kidney mask into the spleen region. A potential explanation is the similar intensity between the spleen and kidney, which may obscure their boundaries. Furthermore, as depicted in Fig. 5 (e), SAM 2 stops propagating the mask after the spleen disappears from the images. This may be because the adjacent lung tissue has a much lower intensity (i.e., darker) in MRI, making the boundary more distinct.

On target-present slices, SLM-SAM 2 achieves an overall better performance compared to SAM 2 in MRI muscle datasets, while maintaining comparable performance across other tasks. By incorporating a dynamic learning mechanism that integrates both short-term and long-term memory, SLM-SAM 2 exhibits improved robustness at target boundaries, significantly mitigating over-propagation problem. We argue that such vague boundary situations are common in medical imaging, like unclear boundaries often occur between the femur and hip bones in CT scans, as shown in Fig. 4. These

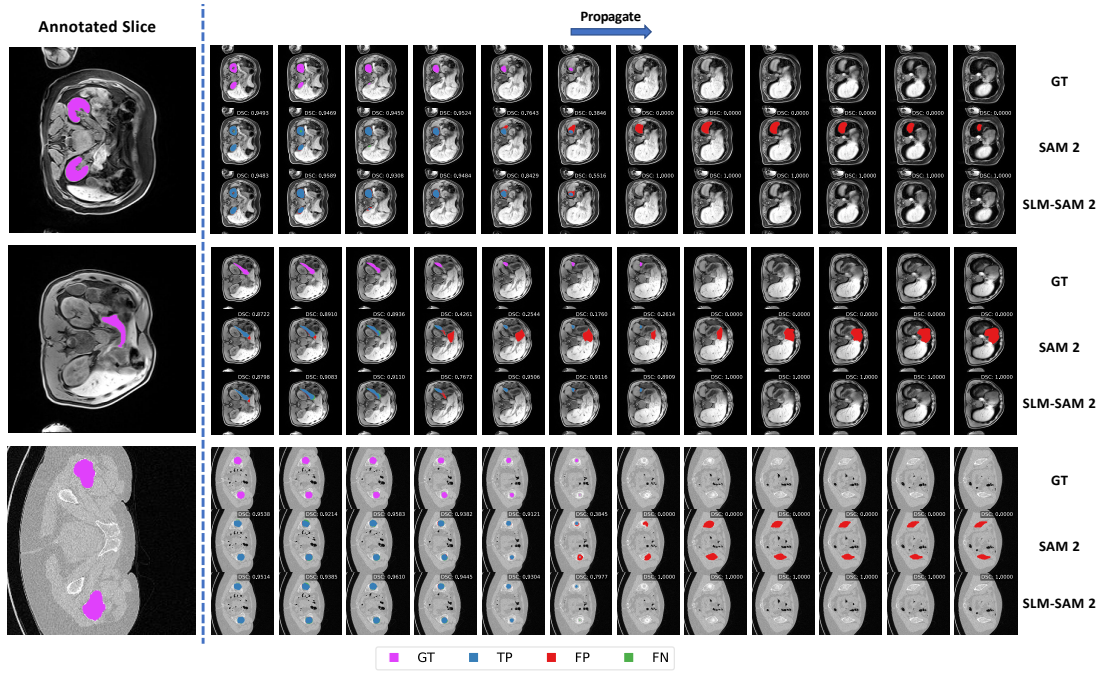


Fig. 6. Qualitative comparison of propagation between SLM-SAM 2 and SAM 2. SLM-SAM 2 performs robust at object boundaries, effectively alleviating over-propagation issue. True positive, false positive and false negative predictions are depicted in blue, red and green.

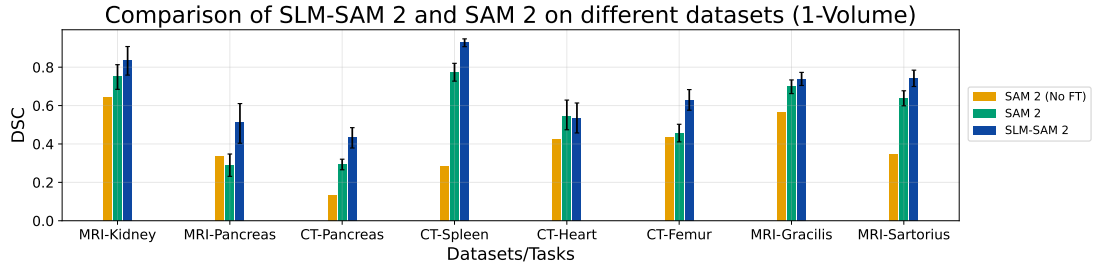


Fig. 7. Performance results (DSC) of SAM 2 and SLM-SAM 2 (1-Volume). SLM-SAM 2 outperforms SAM 2 on most datasets under the 1-Volume settings, excluding CT-Heart, where both methods perform similarly. 5 volumes are randomly selected for each dataset.

Average performance (DSC & ASSD) across all datasets (1-Volume)

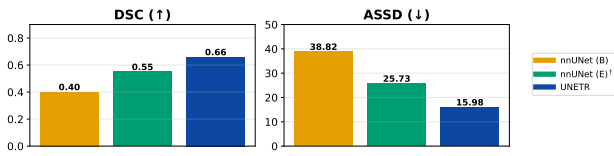


Fig. 8. Average performance comparison across dataset (1-Volume). SLM-SAM 2 shows the better average performance compared with SAM 2 under the 1-Volume setting.

challenges may result from factors such as intensity similarities between the target and neighboring structures, close proximity or direct contact between anatomical structures, and limitations in scan resolution (i.e., slice thickness or spacing between slices). Therefore, the ability of SLM-SAM 2 to better handle boundary ambiguity makes it a promising approach for medical image segmentation.

4) *Experiments on 1-Volume Setting*: In practical scenarios, practitioners may be interested in annotating a single volume and applying the finetuned model on that volume directly to

annotate new data to save time. Thus, we also investigate the performance of SLM-SAM 2 under the 1-Volume setting in comparison with SAM 2. Specifically, we randomly select five different volumes for training and report the average performance of the five models for each dataset. We follow the same training and inference settings as in the 5-Volume experiments, with the same test sets. Fig. 8 shows that SLM-SAM 2 achieves better average performance (DSC: 0.66, ASSD: 15.98) than SAM 2 (DSC: 0.55, ASSD: 25.73), demonstrating that SLM-SAM 2 also provides a more accurate and robust model under the 1-Volume setting. Furthermore, Fig. 7 presents the performance on each dataset, where SLM-SAM 2 consistently outperforms SAM 2 by a significant margin.

5) *Ablation Study*: In this section, we present an ablation study to investigate the impact of different memory bank configurations on model performance. Specifically, we examine how varying the selection and combination of slices within the memory bank influences the results. We denote the baseline SAM 2 configuration as \mathcal{M}_O , which consists of an original memory bank containing one annotated slice and six additional recent slices. Our SLM-SAM 2 is represented as

TABLE II

QUANTITATIVE RESULTS (DSC) OF ABLATION STUDY UNDER THE 5-VOLUME SETTINGS. BEST RESULTS ARE IN BOLD; RUNNER-UP IS UNDERLINED.

			MRI-Kidney	MRI-Pancreas	CT-Pancreas	CT-Spleen	CT-Heart	CT-Femur	MRI-Gracilis	MRI-Sartorius
Methods	\mathcal{M}_1	\mathcal{M}_2	DSC (\uparrow)	DSC (\uparrow)	DSC (\uparrow)	DSC (\uparrow)	DSC (\uparrow)	DSC (\uparrow)	DSC (\uparrow)	DSC (\uparrow)
\mathcal{M}_O (No FT)	\mathcal{M}_O	\times	0.6428	0.3358	0.1345	0.2858	0.4271	0.4359	0.5662	0.3483
\mathcal{M}_O	\mathcal{M}_O	\times	0.8668	0.2341	0.6381	0.9633	0.6925	0.6267	0.7926	0.7045
$\mathcal{M}_R = 7$	$\mathcal{M}_R = 7$	\times	0.9088	0.3009	0.6552	0.9590	0.6650	0.9232	0.7043	0.4989
$\mathcal{M}_R = 1$	$\mathcal{M}_R = 1$	\times	0.9018	<u>0.4866</u>	0.6637	0.9494	0.7138	0.9351	0.7900	<u>0.7882</u>
$\mathcal{M}_O + \mathcal{M}_R = 7$	\mathcal{M}_O	$\mathcal{M}_R = 7$	0.8916	0.3765	0.6690	<u>0.9621</u>	<u>0.7177</u>	<u>0.9559</u>	0.7765	0.6836
$\mathcal{M}_O + \mathcal{M}_R = 1$	\mathcal{M}_O	$\mathcal{M}_R = 1$	0.9368	0.6294	0.7255	0.9607	0.7655	0.9643	0.8543	0.8118

$\mathcal{M}_O + (\mathcal{M}_R = 1)$, which dynamically integrates the original SAM 2 memory bank (\mathcal{M}_O) with a recent memory bank that includes the most recent slice. Furthermore, we evaluate the performance when using only the recent memory bank, considering two configurations: one with the seven most recent slices ($\mathcal{M}_R = 7$) and another with only the single most recent slice ($\mathcal{M}_R = 1$). In addition, we explore the combination of the original memory bank \mathcal{M}_O with the recent bank containing the seven most recent slices, denoted as $\mathcal{M}_O + (\mathcal{M}_R = 7)$.

Average performance of ablation study across all datasets (5-Volume)

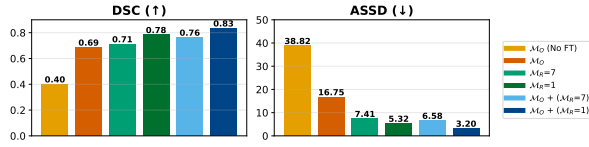


Fig. 9. Average performance comparison of ablation study. SLM-SAM 2 (i.e., $\mathcal{M}_O + (\mathcal{M}_R = 1)$) achieves best results compared with other memory bank configurations in both DSC and ASSD.

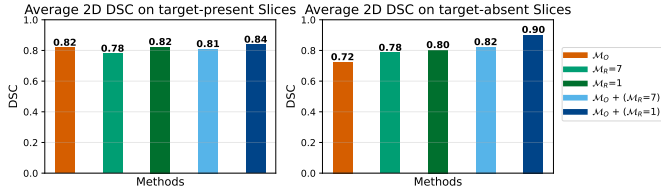


Fig. 10. Average performance results of ablation study on target-present and target-absent slices. SLM-SAM 2 achieves best performance on both target-present and target-absent slices in terms of DSC.

As shown in Fig. 9, it can be seen that using only recent memory (i.e., $\mathcal{M}_R = 7$ and $\mathcal{M}_R = 1$) significantly outperforms \mathcal{M}_O . Specifically, Fig. 10 shows that utilizing recent memory alone achieves superior performance on target-absent slices, with $\mathcal{M}_R = 7$ and $\mathcal{M}_R = 1$ achieving DSC of 0.78 and 0.80, respectively, compared to 0.72 for \mathcal{M}_O . A potential explanation is that retaining annotated slices in the single memory bank (e.g., \mathcal{M}_O) may lead to less robustness at object boundaries and an increased risk of over-propagation errors.

Moreover, we find that combining the original memory bank \mathcal{M}_O with recent memory banks, such as $\mathcal{M}_O + (\mathcal{M}_R = 1)$ and $\mathcal{M}_O + (\mathcal{M}_R = 7)$, results in improved performance compared to using either \mathcal{M}_O or the respective recent memory bank alone (shown in Fig. 9). This demonstrates the effectiveness of the proposed dynamically learned memory mechanism, which integrates information from multiple memory banks.

Notably, as shown in Table II, $\mathcal{M}_O + (\mathcal{M}_R = 1)$ consistently outperforms $\mathcal{M}_O + (\mathcal{M}_R = 7)$, with the exception of CT-Spleen, where both configurations achieve a comparable DSC of approximate 0.96. This finding aligns with our expectations, as combining short-term memory bank ($\mathcal{M}_R = 1$) and \mathcal{M}_O enables the model to leverage both gradual temporal information and direct attention to the most recent slice.

Overall, $\mathcal{M}_O + (\mathcal{M}_R = 1)$ achieves the best performance on both target-present and target-absent slices, highlighting the advance memory mechanism design of SLM-SAM 2.

F. SLM-SAM 2 in 3D Slicer

3D Slicer is an open-source platform for medical image annotation [46]. To integrate SLM-SAM 2 directly into this environment, we have developed a 3D Slicer extension (SegmentHumanBody) that enables interactive inference and mask propagation. Users can load finetuned SLM-SAM 2 checkpoint weights and propagate annotations in bi-directional mode. Generated segmentations may then be refined using 3D Slicer's built-in modules. The extension is available on GitHub at: <https://github.com/mazurowski-lab/SlicerSegmentHumanBody>

V. CONCLUSION

In this paper, we proposed SLM-SAM 2, a novel VOS method to accelerate volumetric medical image annotation by propagating annotations from a single slice to the remaining slices in volumetric medical data. SLM-SAM 2 introduces a dynamic short-long memory module that integrates both short-term and long-term memory, along with a learnable attention fuser. We evaluated SLM-SAM 2 on organs, bones and muscles across three public datasets. Both quantitative and qualitative results have demonstrated the superior performance of SLM-SAM 2 compared to leading automatic 2D and 3D models, as well as unsupervised and supervised VOS methods, effectively alleviating over-propagation issues.

REFERENCES

- [1] M. I. Higgins, J. P. Marquardt, V. A. Master, F. J. Fintelmann, and S. P. Psutka, "Machine learning in body composition analysis," *European Urology Focus*, vol. 7, no. 4, pp. 713–716, 2021.
- [2] H. Gu, R. Colglazier, H. Dong, J. Zhang, Y. Chen, Z. Yildiz, Y. Chen, L. Li, J. Yang, J. Willhite *et al.*, "Segmentanybone: A universal model that segments any bone at any location on mri," *Medical Image Analysis*, p. 103469, 2025.
- [3] Y. Chen, H. Gu, Y. Chen, J. Yang, H. Dong, J. Y. Cao, A. Camarena, C. Mantyh, R. Colglazier, and M. A. Mazurowski, "Automated muscle and fat segmentation in computed tomography for comprehensive body composition analysis," *arXiv preprint arXiv:2502.09779*, 2025.

- [4] O. Ronneberger, P. Fischer, and T. Brox, "U-net: Convolutional networks for biomedical image segmentation," in *Medical image computing and computer-assisted intervention—MICCAI 2015: 18th international conference, Munich, Germany, October 5-9, 2015, proceedings, part III 18*. Springer, 2015, pp. 234–241.
- [5] Y. Chen, H. Zhou, and Z. C. Lipton, "Moco-transfer: Investigating out-of-distribution contrastive learning for limited-data domains," *arXiv preprint arXiv:2311.09401*, 2023.
- [6] H. Dong, H. Gu, Y. Chen, J. Yang, Y. Chen, and M. A. Mazurowski, "Segment anything model 2: an application to 2d and 3d medical images," *arXiv preprint arXiv:2408.00756*, 2024.
- [7] C. Shen, W. Li, Y. Shi, and X. Wang, "Interactive 3d medical image segmentation with sam 2," *arXiv preprint arXiv:2408.02635*, 2024.
- [8] P.-H. Yeung, A. I. Namburete, and W. Xie, "Sli2vol: Annotate a 3d volume from a single slice with self-supervised learning," in *Medical Image Computing and Computer Assisted Intervention—MICCAI 2021: 24th International Conference, Strasbourg, France, September 27–October 1, 2021, Proceedings, Part II 24*. Springer, 2021, pp. 69–79.
- [9] A. Bitarafan, M. F. Azampour, K. Bakhtari, M. Soleymani Baghshah, M. Keicher, and N. Navab, "Vol2flow: segment 3d volumes using a sequence of registration flows," in *International Conference on Medical Image Computing and Computer-Assisted Intervention*. Springer, 2022, pp. 609–618.
- [10] Y. Wu, B. Zheng, J. Chen, D. Z. Chen, and J. Wu, "Self-learning and one-shot learning based single-slice annotation for 3d medical image segmentation," in *International Conference on Medical Image Computing and Computer-Assisted Intervention*. Springer, 2022, pp. 244–254.
- [11] D. An, P. Gu, M. Sonka, C. Wang, and D. Z. Chen, "Sli2vol+: Segmenting 3d medical images based on an object estimation guided correspondence flow network," *arXiv preprint arXiv:2411.13873*, 2024.
- [12] N. Ravi, V. Gabeur, Y.-T. Hu, R. Hu, C. Ryali, T. Ma, H. Khedr, R. Rädle, C. Rolland, L. Gustafson *et al.*, "Sam 2: Segment anything in images and videos," *arXiv preprint arXiv:2408.00714*, 2024.
- [13] A. Kirillov, E. Mintun, N. Ravi, H. Mao, C. Rolland, L. Gustafson, T. Xiao, S. Whitehead, A. C. Berg, W.-Y. Lo *et al.*, "Segment anything," in *Proceedings of the IEEE/CVF International Conference on Computer Vision*, 2023, pp. 4015–4026.
- [14] M. A. Mazurowski, H. Dong, H. Gu, J. Yang, N. Konz, and Y. Zhang, "Segment anything model for medical image analysis: an experimental study," *Medical Image Analysis*, vol. 89, p. 102918, 2023.
- [15] R. Yao, G. Lin, S. Xia, J. Zhao, and Y. Zhou, "Video object segmentation and tracking: A survey," *ACM Transactions on Intelligent Systems and Technology (TIST)*, vol. 11, no. 4, pp. 1–47, 2020.
- [16] Z. Yildiz, Y. Chen, and M. A. Mazurowski, "Sam & sam 2 in 3d slicer: Segmentwithsam extension for annotating medical images," *arXiv preprint arXiv:2408.15224*, 2024.
- [17] S. Asgari Taghanaki, K. Abhishek, J. P. Cohen, J. Cohen-Adad, and G. Hamarneh, "Deep semantic segmentation of natural and medical images: a review," *Artificial Intelligence Review*, vol. 54, pp. 137–178, 2021.
- [18] Y. Xu, R. Quan, W. Xu, Y. Huang, X. Chen, and F. Liu, "Advances in medical image segmentation: A comprehensive review of traditional, deep learning and hybrid approaches," *Bioengineering*, vol. 11, no. 10, p. 1034, 2024.
- [19] F. Isensee, P. F. Jaeger, S. A. Kohl, J. Petersen, and K. H. Maier-Hein, "nnu-net: a self-configuring method for deep learning-based biomedical image segmentation," *Nature methods*, vol. 18, no. 2, pp. 203–211, 2021.
- [20] J. W. Kim, A. U. Khan, and I. Banerjee, "Systematic review of hybrid vision transformer architectures for radiological image analysis," *medRxiv*, pp. 2024–06, 2024.
- [21] A. Dosovitskiy, "An image is worth 16x16 words: Transformers for image recognition at scale," *arXiv preprint arXiv:2010.11929*, 2020.
- [22] J. Wu, W. Ji, Y. Liu, H. Fu, M. Xu, Y. Xu, and Y. Jin, "Medical sam adapter: Adapting segment anything model for medical image segmentation," *arXiv preprint arXiv:2304.12620*, 2023.
- [23] X. Wang, L. Liu, X. Su, Y. Yang, and G. Gao, "Fsam: Fine-tuning sam encoder and decoder for medical image segmentation," in *2024 IEEE International Conference on Bioinformatics and Biomedicine (BIBM)*. IEEE, 2024, pp. 5569–5573.
- [24] M. Siam, A. Kendall, and M. Jagersand, "Video class agnostic segmentation benchmark for autonomous driving," in *Proceedings of the IEEE/CVF Conference on Computer Vision and Pattern Recognition*, 2021, pp. 2825–2834.
- [25] M. Kozłowski, S. Racewicz, and S. Wierzbicki, "Image analysis in autonomous vehicles: A review of the latest ai solutions and their comparison," *Applied Sciences*, vol. 14, no. 18, p. 8150, 2024.
- [26] B. Miao, M. Bennamoun, Y. Gao, and A. Mian, "Region aware video object segmentation with deep motion modeling," *IEEE Transactions on Image Processing*, 2024.
- [27] N. Manakitsa, G. S. Maraslidis, L. Moysis, and G. F. Fragulis, "A review of machine learning and deep learning for object detection, semantic segmentation, and human action recognition in machine and robotic vision," *Technologies*, vol. 12, no. 2, p. 15, 2024.
- [28] J. Zhu, Y. Qi, and J. Wu, "Medical sam 2: Segment medical images as video via segment anything model 2," *arXiv preprint arXiv:2408.00874*, 2024.
- [29] M. Gao, F. Zheng, J. J. Yu, C. Shan, G. Ding, and J. Han, "Deep learning for video object segmentation: a review," *Artificial Intelligence Review*, vol. 56, no. 1, pp. 457–531, 2023.
- [30] T. Zhou, F. Porikli, D. J. Crandall, L. Van Gool, and W. Wang, "A survey on deep learning technique for video segmentation," *IEEE transactions on pattern analysis and machine intelligence*, vol. 45, no. 6, pp. 7099–7122, 2022.
- [31] H. K. Cheng, S. W. Oh, B. Price, J.-Y. Lee, and A. Schwing, "Putting the object back into video object segmentation," in *Proceedings of the IEEE/CVF Conference on Computer Vision and Pattern Recognition*, 2024, pp. 3151–3161.
- [32] M. Aljabri, M. AlAmir, M. AlGhamdi, M. Abdel-Mottaleb, and F. Collado-Mesa, "Towards a better understanding of annotation tools for medical imaging: a survey," *Multimedia tools and applications*, vol. 81, no. 18, pp. 25 877–25 911, 2022.
- [33] S. Wang, C. Li, R. Wang, Z. Liu, M. Wang, H. Tan, Y. Wu, X. Liu, H. Sun, R. Yang *et al.*, "Annotation-efficient deep learning for automatic medical image segmentation," *Nature communications*, vol. 12, no. 1, p. 5915, 2021.
- [34] L. Bonaldi, A. Pretto, C. Pirri, F. Uccheddu, C. G. Fontanella, and C. Stecco, "Deep learning-based medical images segmentation of musculoskeletal anatomical structures: a survey of bottlenecks and strategies," *Bioengineering*, vol. 10, no. 2, p. 137, 2023.
- [35] R. Feng, X. Zheng, T. Gao, J. Chen, W. Wang, D. Z. Chen, and J. Wu, "Interactive few-shot learning: Limited supervision, better medical image segmentation," *IEEE Transactions on Medical Imaging*, vol. 40, no. 10, pp. 2575–2588, 2021.
- [36] E. Pachetti and S. Colantonio, "A systematic review of few-shot learning in medical imaging," *Artificial intelligence in medicine*, p. 102949, 2024.
- [37] W. Xie, N. Willems, S. Patil, Y. Li, and M. Kumar, "Sam fewshot fine-tuning for anatomical segmentation in medical images," in *Proceedings of the IEEE/CVF Winter Conference on Applications of Computer Vision*, 2024, pp. 3253–3261.
- [38] J. Ma, Y. He, F. Li, L. Han, C. You, and B. Wang, "Segment anything in medical images," *Nature Communications*, vol. 15, no. 1, p. 654, 2024.
- [39] A. Hatamizadeh, Y. Tang, V. Nath, D. Yang, A. Myronenko, B. Landman, H. R. Roth, and D. Xu, "Unetr: Transformers for 3d medical image segmentation," in *Proceedings of the IEEE/CVF winter conference on applications of computer vision*, 2022, pp. 574–584.
- [40] A. Hatamizadeh, V. Nath, Y. Tang, D. Yang, H. R. Roth, and D. Xu, "Swin unetr: Swin transformers for semantic segmentation of brain tumors in mri images," in *International MICCAI brainlesion workshop*. Springer, 2021, pp. 272–284.
- [41] J. Wasserthal, H.-C. Breit, M. T. Meyer, M. Pradella, D. Hinck, A. W. Sauter, T. Heye, D. T. Boll, J. Cyriac, S. Yang *et al.*, "Totalsegmentator: robust segmentation of 104 anatomic structures in ct images," *Radiology: Artificial Intelligence*, vol. 5, no. 5, 2023.
- [42] Z. Liu, H. Mao, C.-Y. Wu, C. Feichtenhofer, T. Darrell, and S. Xie, "A convnet for the 2020s," in *Proceedings of the IEEE/CVF conference on computer vision and pattern recognition*, 2022, pp. 11 976–11 986.
- [43] Y. Ji, H. Bai, C. GE, J. Yang, Y. Zhu, R. Zhang, Z. Li, L. Zhanng, W. Ma, X. Wan, and P. Luo, "Amos: A large-scale abdominal multi-organ benchmark for versatile medical image segmentation," 2022.
- [44] H. Zhong, "Hirriririr/multimodal-multiethnic-thigh-muscle-mri-analysis," 6 2023. [Online]. Available: <https://github.com/Hirriririr/multimodal-Multiethnic-Thigh-Muscle-MRI-analysis>
- [45] G. Balakrishnan, A. Zhao, M. R. Sabuncu, J. Guttag, and A. V. Dalca, "Voxelmorph: a learning framework for deformable medical image registration," *IEEE transactions on medical imaging*, vol. 38, no. 8, pp. 1788–1800, 2019.
- [46] A. Fedorov, R. Beichel, J. Kalpathy-Cramer, J. Finet, J.-C. Fillion-Robin, S. Pujol, C. Bauer, D. Jennings, F. Fennessy, M. Sonka *et al.*, "3d slicer as an image computing platform for the quantitative imaging network," *Magnetic resonance imaging*, vol. 30, no. 9, pp. 1323–1341, 2012.